International Forum on Aeroelasticity and Structural Dynamics
IFASD 2026
17-21 June 2026, Goettingen, Germany

HAP-ALPHA: FLIGHT CONTROL DESIGN CONSIDERING STRUCTURE AND RIGID-BODY COUPLING

Christian Weiser[1] **and Thiemo M. Kier**[2]

[1]Institute of Flight Systems, German Aerospace Center (DLR)
Münchener Str. 20, 82234 Weßling, Germany
christian.weiser@dlr.de

[2]Institute of Aeroelasticity, German Aerospace Center (DLR)
Münchener Str. 20, 82234 Weßling, Germany
thiemo.kier@dlr.de

Keywords: Flight Control Design, DLR HAP-alpha

Abstract: High-Altitude Long-Endurance (HALE) aircraft are designed for extended stratospheric operations, necessitating ultra-lightweight structures that introduce complex aeroelastic effects. For such HALE platforms, traditional flight control design approaches, which typically decouple primary flight control design from load mitigation, are compromised by the spectral overlap and interaction between rigid-body and structural modes. This paper presents a flight control design process for the German Aerospace Center's *HAP-alpha* configuration that explicitly accounts for structure and rigid-body coupling. A flexible aircraft model is utilized to synthesize a gain-scheduled controller using structured H_∞ methods. The control architecture comprises a cascaded loop structure with inner-loop rate-command-attitude-hold capabilities and an integrated envelope protection system that dynamically enforces airspeed limits. The proposed design is verified through frequency-domain analysis and nonlinear, high-fidelity software-in-the-loop simulations. Furthermore, the flight control system is cleared against certification-level disturbance scenarios using Monte Carlo analysis and optimization-based worst-case search, demonstrating robust performance and structural protection.

1 INTRODUCTION

High Altitude Long Endurance (HALE) aircraft represent a promising class of unmanned platforms capable of sustained operations in the stratosphere at altitudes up to 25 km. Designed for missions that require continuous airborne presence spanning multiple days to several months, these platforms offer satellite-like capabilities at significantly lower deployment and operational costs. To achieve such extreme endurance, HALE vehicles are typically powered exclusively by solar energy and rely on exceptionally lightweight structures. This structural efficiency fundamentally alters the aeroelastic characteristics of the airframe, resulting in high structural flexibility, low tolerance to external aerodynamic disturbances, unusually low cruise airspeed, and a highly constrained flight envelope.

Conventional flight control design methodologies for large transport aircraft typically rely on a decoupled approach, separating primary attitude control from secondary load-mitigation functions. The distinct spectral gap between rigid-body dynamics and high-frequency structural modes justifies this separation. For very lightweight and highly flexible HALE platforms, however, this assumption breaks down. The low airspeed and extreme structural compliance cause

Figure 1: DLR HAP-alpha aircraft rendering (©DLR).

significant overlap between the rigid-body short-period modes and the low-frequency bending and torsional structural modes. Consequently, traditional control architectures struggle to simultaneously ensure stable attitude tracking, satisfy certification requirements, and mitigate structural loads without inducing harmful aeroelastic interactions.

Addressing these coupled dynamics requires a holistic design framework that explicitly accounts for the interaction between rigid-body motion and flexible structural modes from the outset. This paper presents a comprehensive flight control design process for the German Aerospace Center's (DLR's) High-Altitude Platform configuration, *HAP-alpha*, which integrates structural flexibility directly into the control synthesis and verification loop. Unlike conventional approaches that treat flexibility as a minor perturbation, our methodology employs a fully flexible aircraft model to capture the bidirectional coupling between aerodynamics, structural dynamics, and rigid-body motion. The resulting control architecture utilizes a gain-scheduled, fixed-structure framework synthesized via structured H_∞ methods [1], incorporating an envelope protection layer that dynamically enforces airspeed and angle of attack (AoA) limits during augmented flight.

The proposed design is rigorously verified through a multi-stage clearance process. Initial frequency-domain assessments evaluate control performance, robustness, and structural load rejection. These results are subsequently verified in a high-fidelity, nonlinear software-in-the-loop (SIL) simulation environment, which incorporates detailed actuator dynamics, sensor noise, propulsion models, and realistic atmospheric disturbance profiles, including 1-cosine discrete gust loads. Statistical clearance margins are assessed using Monte Carlo (MC) simulations, while deterministic worst-case optimization identifies conservative load multipliers for structural design.

The paper is organized into three primary sections: Section 2 details the flexible aircraft modeling approach, including enhancements on modeling aerodynamic drag within the Vortex Lattice Method (VLM). Section 3 outlines the cascaded control architecture and robust synthesis procedure, and Section 4 describes the multi-fidelity verification process and presents the simulation results.

2 FLEXIBLE AIRCRAFT MODEL

For the design of the flight control software (FCSW), a flexible flight dynamics model has been implemented based on the model data in references [2, 3]. The model uses standard flight mechanics equations of motion [4] as implemented, e.g., in the DLR VarLoads toolchain [5].

The equations of motion used are based on a *mean axes* formulation [4], including nonlinear rigid-body motion as well as linear structural dynamics.

$$\begin{bmatrix} \mathbf{m}_b \left(\dot{\mathbf{V}}_b(t) + \mathbf{\Omega}_b(t) \times \mathbf{V}_b(t) - \mathbf{T}_{bE}(t)\, \mathbf{g}_E\right) \\ \mathbf{J}_b \dot{\mathbf{\Omega}}_b(t) + \mathbf{\Omega}_b(t) \times (\mathbf{J}_b \mathbf{\Omega}_b(t)) \end{bmatrix} = \mathbf{\Phi}_{gb}^{\mathrm{T}} \mathbf{P}_g^{\mathrm{ext}}(t)$$
$$\mathbf{M}_{\mathit{ff}} \ddot{\mathbf{u}}_f(t) + \mathbf{B}_{\mathit{ff}} \dot{\mathbf{u}}_f(t) + \mathbf{K}_{\mathit{ff}} \mathbf{u}_f(t) = \mathbf{\Phi}_{\mathit{gf}}^{\mathrm{T}} \mathbf{P}_g^{\mathrm{ext}}(t), \tag{1}$$

where $\mathbf{\Phi}_{gb}$ is the rigid-body modal matrix about the center of gravity and in directions as customary in flight mechanics, i.e., x-forward, z-down. $\mathbf{V}_b$ and $\mathbf{\Omega}_b$ are, respectively, the velocity and angular velocity vectors in the body frame of reference. The matrix $\mathbf{T}_{bE}$ transforms the gravitational vector from an earth-fixed (E) to the body-fixed coordinate frame (b) as a function of Euler angles. The inertial tensor $\mathbf{J}_b$ and the aircraft mass $\mathbf{m}_b$ can be obtained from the 6×6 mass matrix $\mathbf{M}_{bb} = \mathbf{\Phi}_{gb}^{\mathrm{T}}\, \mathbf{M}_{gg}\, \mathbf{\Phi}_{gb}$. The flexible modal mass $\mathbf{M}_{\mathit{ff}}$ and stiffness $\mathbf{K}_{\mathit{ff}}$ are obtained accordingly. The equations of motion are driven by the external forces $\mathbf{P}_g^{ext}$. These are noted in the structural grid point coordinates ($g-\mathrm{set}$). Sources of these external loads are the propulsion system and the aerodynamic forces. For the calculation of aerodynamic forces, the VLM is used with enhancements featuring a more realistic drag model [6].

Additionally, via the force summation method [7], load recovery can be executed. This enables the analysis of structural loads at various cut-points within the aircraft in the post-processing. Additionally, the load monitoring stations can be set as an output during linearization. This possibility can be used later in the verification framework to determine the influences of the controller on the peak structural loads.

2.1 Quasi-Steady Aerodynamics: Vortex Lattice Method

The large number of design analysis cases required in many aircraft design disciplines is still prohibitive for the widespread adoption of costly Computational Fluid Dynamics–Computational Structural Mechanics (CFD-CSM) coupled calculations. Therefore, classical methods derived from potential theory, such as the VLM [8], remain widely used for flexible aircraft dynamics applications.

The VLM discretizes a lifting surface into trapezoidal-shaped elementary wings, so-called aerodynamic boxes. A vortex is placed along the quarter-chord line of each aerodynamic box to generate aerodynamic lift. According to the Helmholtz theorems, such a vortex must either end at a solid surface or extend to infinity. Hence, the bound vortex is extended at both corner points to infinity, forming the well-known horseshoe shape with its legs pointing in the free stream direction. The circulation strengths $\mathbf{\Gamma}_j$ of the individual horseshoe vortices are then determined by the Biot-Savart Law and by meeting the flow compatibility condition, i.e., no perpendicular flow $\mathbf{v}_j$ through the solid surface at the control points at $3/4$ chord, according to Pistolesi's theorem [9].

$$\mathbf{v}_j = \mathbf{A}_{jj} \mathbf{\Gamma}_j \tag{2}$$

Figure 2 depicts the geometry of an aerodynamic box. The load acting point is located at mid span, quarter-chord ($l-\mathrm{set}$), and the control point at the three-quarter-chord point ($j-\mathrm{set}$), respectively. The box reference point ($k-\mathrm{set}$) is at the center of the box. The panel chord is c_j, and the span is b_j. The vector of the bound vortex is denoted by $\mathbf{b}_l$.

The Kutta-Joukowski Law relates the circulation to the lifting force.

$$L_j = \rho U_\infty \Gamma_j b_j \tag{3}$$

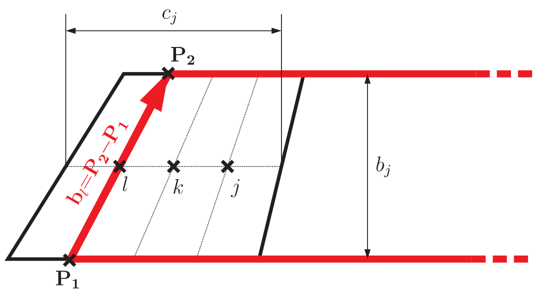

Figure 2: Geometrical properties of an aerodynamic box

Normalizing the velocities at the control point $\mathbf{w}_j = \frac{\mathbf{v}_j}{U_\infty}$ and inversion of Eq. (2), yields the differential pressure coefficients with the aerodynamic AIC matrix.

$$\Delta \mathbf{c}_{\mathbf{p}_j} = \mathbf{Q}_{jj}\mathbf{w}_j \tag{4}$$

Conversely, the circulation of an individual horseshoe vortex can be calculated from the pressure coefficient as follows.

$$\Gamma_j = U_\infty \frac{c_j}{2} \Delta c_{p_j} \tag{5}$$

This is the standard implementation of the VLM as employed, for instance, in the aeroelastic solutions of `NASTRAN` [10]. In the degree of freedom (DoF) notation for the $j-$,$k-$, and $l-$set, this implies :

$$\mathbf{u}_j = \begin{bmatrix} z \end{bmatrix}_j \;;\; \mathbf{u}_k = \begin{bmatrix} z & \theta \end{bmatrix}_k^{\mathrm{T}} \;;\; \mathbf{u}_l = \begin{bmatrix} z \end{bmatrix}_l \tag{6}$$

The boundary condition must be met at the $3/4$ chord location in the z-direction ($j-\text{set}$). The resulting lift in the $l-\text{set}$ also acts in the z-direction of the box geometry at the quarter-chord, resulting in an additional moment about the y-axis when regarding the box reference location $k-\text{set}$.

Alternatively, the Kutta-Joukowski-Law can be cast in the following form, involving a cross product instead of a scalar multiplication. This approach was proposed in [11] to enhance the flexible aircraft models for load analysis.

$$\mathbf{L}_l = \rho \mathbf{V}_l \times (\mathbf{b}_l \Gamma_j) \quad \text{with } \mathbf{L}_l, \mathbf{V}_l, \mathbf{b}_l \in \mathbb{R}^3 \text{ and } \Gamma_j \in \mathbb{R}^1 \tag{7}$$

The vector $\mathbf{b}_l$ is the vector quantity between the two corners of the horseshoe vortex, i.e., the bound vortex. The lift force $\mathbf{L}_l$ then acts, as aerodynamic theory predicts, perpendicular to the local stream velocity $\mathbf{V}_l$ at the quarter-chord point. Consequently, the DoF-sets have to be extended:

$$\mathbf{u}_j = \begin{bmatrix} z \end{bmatrix}_j \;;\; \mathbf{u}_k = \begin{bmatrix} x & y & z & \varphi & \theta & \psi \end{bmatrix}_k^{\mathrm{T}} \;;\; \mathbf{u}_l = \begin{bmatrix} x & y & z \end{bmatrix}_l^{\mathrm{T}} \tag{8}$$

The lift at the quarter-chord ($l-\text{set}$) is now a vector quantity in all three translational directions. The $k-\text{set}$ at the reference point was extended to all six DoFs to account for moments arising from the directional lift.

Eq. (7) can now be recast in matrix form by using Eq. (5) and the skew matrix operator $\mathbf{sk}()$ for the cross product.

$$\mathbf{L}_l = q_\infty \left(\left[-\mathbf{sk}(\mathbf{b}_l) \right] \mathbf{w}_l \right) \odot \left(c_j \begin{bmatrix} 1 & 1 & 1 \end{bmatrix}^{\mathrm{T}} \Delta c_{p_j} \right) \tag{9}$$

The vector $\mathbf{w}_l$ is the velocity at quarter-chord normalized by the free stream velocity. On the individual box level, the quantities with index l are elements in $\mathbb{R}^3$, whereas index j denotes elements in $\mathbb{R}^1$. The operator $\odot$ in Eq. (9) refers to an elementwise multiplication. A block-diagonal extension of Eq. (9) allows the use of the full DoF vectors in the $l-$ respectively $j-\mathrm{set}$. Since both $\mathbf{w}_l$, as well as $\mathbf{w}_j$ (respectively Δc_{p_j}), depend on the boundary conditions, expression Eq. (9) is inherently nonlinear. Therefore, it is computationally more expensive compared to the linear expression in Eq. (3). If $\mathbf{w}_l = \begin{bmatrix}1 & 0 & 0\end{bmatrix}^{\mathrm{T}}$, i.e., the free stream is assumed to be exclusively in the x-direction, the analysis simplifies to the conventional case, with the lift $\mathbf{L}_l$ acting in the z-direction only.

In a last step, the lift vector $\mathbf{L}_l$ at the quarter-chord is transformed to the reference point at the aerodynamic box center.

$$\mathbf{P}_k^{\mathrm{aero}} = \mathbf{T}_{lk}^{\mathrm{T}}\,\mathbf{L}_l \tag{10}$$

As mentioned before, the $k-\mathrm{set}$ has been extended to full 6-DoF to recover moments arising from the now directional lift vector.

2.2 Boundary Conditions: Differentiation Matrices

The boundary conditions for the VLM are obtained with respect to a box reference point. Depending on the displacement, respectively motion of the reference point, the normal velocity $\mathbf{w}_j$ at the control point and velocity at the quarter-chord point $\mathbf{w}_l$ need to be determined. The rotational displacement about the transverse axis contributes to the box AoA. The heaving motion, as well as rotational motion due to the offset of the reference point to the control point, also contribute to the effective box AoA.

These contributions can be accounted for by a differentiation with respect to the x-direction (i.e., the slope change θ_k), and the time derivatives of the normalized heaving motion $\dot{z}_k/U_\infty$ and pitching motion $\dot{\theta}_k/U_\infty$. These deformations and motions are represented in the vectors $\mathbf{u}_k$ and $\dot{\mathbf{u}}_k$. Thus, in matrix form, this can be expressed as

$$\mathbf{w}_j = \mathbf{D^x}_{jk}\cdot\mathbf{u}_k \;+\; \mathbf{D^t}_{jk}\left(\tfrac{c_{ref}/2}{U_\infty}\right)\cdot\dot{\mathbf{u}}_k \tag{11}$$

The differentiation matrices are defined as

$$\mathbf{D^x}_{jk} = \begin{bmatrix}0 & 0 & 0 & 0 & 1 & 0\end{bmatrix} \tag{12}$$

and

$$\mathbf{D^t}_{jk} = -\tfrac{2}{c_{ref}}\begin{bmatrix}n_x & 0 & n_z & 0 & -c_j/4 & 0\end{bmatrix}. \tag{13}$$

To account for camber and incidence, the quantities n_x and n_z are the components of the normal vector at the control point. The classical implementation omits the component in the x-direction, i.e., $n_x = 0$ and $n_z = 1$, and merely treats camber as an addition to the differential pressure. In the present implementation, an in-plane motion results in an increased circulation.

The differentiation matrix $\mathbf{D^t}_{lk}$ is set up equivalently for the three translational DoFs at the quarter-chord.

$$\mathbf{w}_l = \mathbf{D^t}_{lk}\left(\tfrac{c_{ref}/2}{U_\infty}\right)\cdot\dot{\mathbf{u}}_k \tag{14}$$

with

$$\mathbf{D^t}_{lk} = -\tfrac{2}{c_{ref}}\begin{bmatrix}1 & 0 & 0 & 0 & 0 & 0\\ 0 & 1 & 0 & 0 & 0 & -c_j/4\\ 0 & 0 & 1 & 0 & c_j/4 & 0\end{bmatrix} \tag{15}$$

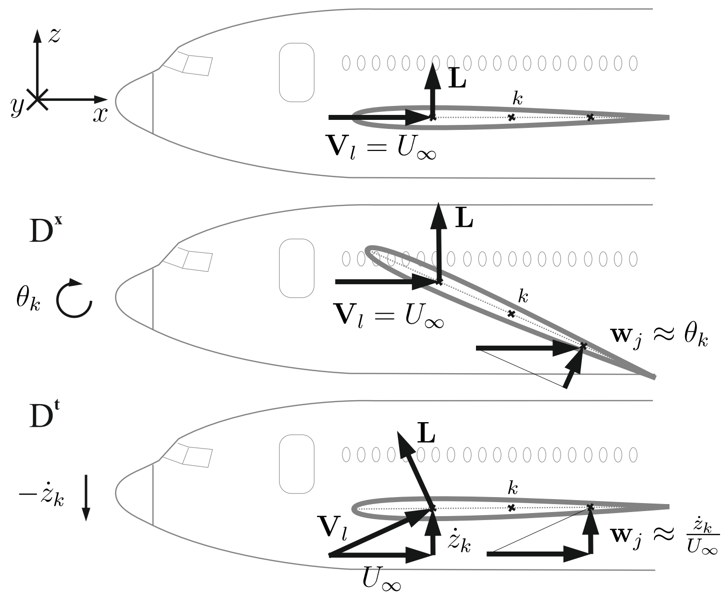

Figure 3: Illustration of the differentiation matrices $\mathbf{D^x}_{jk}$, $\mathbf{D^t}_{jk}$, and $\mathbf{D^t}_{lk}$

Figure 3 illustrates the effects computed by Eqs. (11) and (14).

There is no matrix for $\mathbf{D^x}_{lk}$, as a steady deformation does not change the direction of flow. However, the heaving motion changes the direction of the lift vector. In the classical VLM implementation, this contribution is neglected.

2.3 Induced Drag

Aerodynamic lift is generated by circulation Γ over the wing. Since the circulation distribution of a finite wing must go to zero at the wing tips, a spanwise gradient in circulation results. Induced drag is generated by this spanwise change of the circulation of a 3D lifting surface, which leads to trailing vortices that are shed into the wake. The streamwise vorticity in the wake induces an additional downwash, Eq. (16), on the wing, which turns the lift vector rearward by the induced AoA, Eq. (17). Figure 4 shows the effect on an airfoil section of a finite wing.

Induced downwash is obtained by the integral equation:

$$w_i(y) = -\frac{1}{4\pi}\int_{-b/2}^{b/2} \frac{\mathrm{d}\Gamma(y_0)}{\mathrm{d}y}\frac{\mathrm{d}y_0}{y - y_0} \tag{16}$$

Using a small-angle assumption, the induced AoA is then given by

$$\alpha_i(y) \approx \frac{-w_i(y)}{U_\infty}. \tag{17}$$

The overall induced drag can then be obtained by integrating over the wingspan,

$$D_i = \frac{1}{2}\rho U_\infty \int_{-b/2}^{b/2} \Gamma(y)\alpha_i(y)\ \mathrm{d}y. \tag{18}$$

Similarly, the total lift is obtained by

$$L = \rho U_\infty \int_{-b/2}^{b/2} \Gamma(y)\ \mathrm{d}y. \tag{19}$$

When comparing the integral equations, it can be seen that the lift Eq. (19) depends linearly on the overall circulation Γ, only. Whereas, in the drag integral Eq. (18), the induced AoA α_i is also a function of the circulation Γ, leading to the classical parabola shape of the drag polar.

To obtain the drag forces for the VLM, there are two options:

- **Far-field implementation:** Solving the integral Eqs. (18) and (19) in the so-called Trefftz plane, which is located far downstream and perpendicular to the wake. The integration is carried out along the wake surface in this plane.
- **Near-field implementation:**
  Determining the induced downwash at the quarter-chord point of each box, turning the local lift vectors as depicted in Figure 4.

The near-field implementation is very attractive, as the flexible aircraft equations of motion Eq. (1) require a distributed aerodynamic loading. One drawback of it is that it is somewhat sensitive to the discretization of the lifting surface.

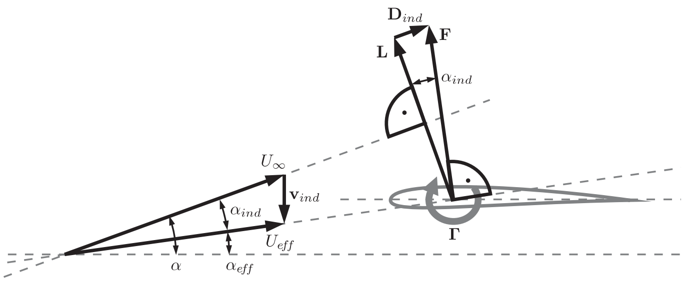

Figure 4: Illustration of induced drag and induced AoA.

Near-Field Induced Drag. The vorticity of the trailing vortices in the wake induces an additional downwash at the quarter-chord of each box, which rotates the lift vector rearward. The sum of the rearward component of all boxes constitutes the induced drag. To evaluate the induced velocities at the quarter-chord point, once again, the Biot-Savart Law is employed. The contribution of the bound vortex of the current box itself needs to be omitted, due to the singularity at zero distance. The three velocity components normalized by the free stream velocity are collected in the vector $\mathbf{w}_{l_{\text{ind}}}$. Similarly to Eq. (2), this operation can be expressed as a matrix equation.

$$\mathbf{w}_{l_{\text{ind}}} = \mathbf{A}_{lj} \frac{\Gamma_j}{U_\infty} \tag{20}$$

To build up the effective stream direction $\mathbf{w}_l$, the induced component $\mathbf{w}_{l_{\text{ind}}}$ is added to the free stream and motion induced components of Eq. (14). The subsequent force calculation in Eq. (9) then includes the induced drag components.

2.4 Interconnection of Aerodynamics with the Equations of Motion

The aerodynamic loads of Eq. (10) are given in the $k - \text{set}$ and have to be mapped to the structural DoFs in the $g - \text{set}$. The matrix connecting the displacements of these two grids is the so-called spline matrix $\mathbf{T}_{kg}$.

$$\mathbf{u}_k = \mathbf{T}_{kg}\, \mathbf{u}_g \tag{21}$$

This mapping can be achieved by employing radial basis functions such as the Infinite Plate Spline (IPS) [12]. It is important to note that the spline must be extended to all six DoFs in the case of directional lift vectors.

The aerodynamic loads can be mapped back onto the structure with the transpose of the spline matrix, based on the principle of virtual work.

$$\mathbf{P}_g^{\text{aero}} = \mathbf{T}_{kg}^{\text{T}}\,\mathbf{P}_k^{\text{aero}} \tag{22}$$

The deflections of the aerodynamic DoFs can then be expressed as

$$\mathbf{u}_k = \mathbf{\Phi}_{kx}\mathbf{u}_x + \mathbf{T}_{kg}\;\mathbf{\Phi}_{gf}\mathbf{u}_f, \tag{23}$$

where $\mathbf{u}_x$ denotes control surface deflections with $\mathbf{\Phi}_{kx}$ defining a rotation about a hinge vector of the aerodynamic boxes belonging to the individual control surfaces. Accordingly, the aerodynamic box velocities are given by

$$\dot{\mathbf{u}}_k = \mathbf{\Phi}_{kx}\dot{\mathbf{u}}_x + \mathbf{T}_{kg}\;\mathbf{\Phi}_{gf}\dot{\mathbf{u}}_f + \mathbf{T}_{kg}\;\mathbf{\Phi}_{gb}\dot{\mathbf{u}}_b. \tag{24}$$

The vector $\dot{\mathbf{u}}_b$ denotes the rigid-body velocity components and rates about the center of gravity in the body axis system. The aerodynamic grid deflections and motions are then used in Eqs. (11) and (14) to obtain the aerodynamic loads.

3 FLIGHT CONTROL DESIGN

The flight control design for the *HAP-alpha* aircraft is based on robust H_∞ synthesis methods [13, 14]. For the design, the linearized models obtained in Section 2 are used: the overall equations of motion with the aerodynamic forcing terms in Eq. (1) represent a nonlinear system of ordinary differential equations:

$$\begin{aligned} \dot{x} &= f(x,u) \\ y &= g(x,u) \end{aligned} \tag{25}$$

For the control design, the model is linearized at different steady-state flight conditions. For all of those operating points, an equilibrium state is assumed, i.e., all forces and moments must be balanced. The most prominent equilibrium state is the horizontal flight, but also any other flight state that constitutes a solution to the system is valid, e.g., pull-up or climb maneuvers. Mathematically, the nonlinear system of equations in Eq. (25) needs to be solved, where the states x, state derivatives $\dot{x}$, inputs u, and outputs y can be either free or constraint variables. To compute a valid solution, the number of free variables must equal the number of equations of the given system. The inputs are generally the control surface deflections, which are allocated to issue roll, pitch, yaw commands, and the engine thrust setting. The trim solution defines the initial conditions x_0 and u_0 for the simulation. When the nonlinear aircraft model is linearized around the given trim state, a linear state space system can be obtained. An eigenvalue analysis of the system matrix yields the root locus of the flexible and flight-dynamical modes with their associated damping ratios and frequencies.

The above-presented nonlinear model serves for:

1. Generating linear models of the form

$$\left[\begin{array}{c} \dot{x} \\ \hline y \end{array}\right] = \left[\begin{array}{c|cc} A & B_u & B_d \\ \hline C & D_u & D_d \end{array}\right] \left[\begin{array}{c} x \\ \hline u \\ d \end{array}\right] \tag{26}$$

which are used for linear control design using robust control design methods. The vector x denotes the state vector, including relevant rigid-body and flexible states, u is the control input, i.e., control surface deflection angles, y denotes the output vector, and d is the disturbance input vector. The disturbance vector contains disturbances in AoA and angle of sideslip, and these disturbances can be used to tune the disturbance rejection properties of the controller.

2. The nonlinear model is used for simulations in the SIL environment to evaluate the control laws.

The nonlinear aircraft equations are linearized at steady-state operating points defined by equivalent airspeed V_{eas} and altitude h. The grid points are spaced equidistantly ($2\,\mathrm{m/s}$ apart) between stall speed V_s and maximum airspeed V_{ne}. In the altitude dimension, the range is between Flight Level (FL)0 and FL800 spaced 100 FL apart (corresponding to $3048\,\mathrm{m}$).

3.1 Flight Dynamic Model Analysis

This section transforms the nonlinear flexible aircraft model into linear models for the flight control design. The procedure is executed for the model with the standard VLM implementation and for the model version using the updated VLM drag implementation described in Section 2.3. The differences that arise due to the implementation of induced drag are shown for two examples, namely the Phugoid and Dutch Roll eigenmodes.

Figure 5 shows the Phugoid pole locations of the aircraft model implementations at one altitude (sea level). The updated VLM version, including induced drag, shows a more realistic variation of the Phugoid poles over airspeed, as damping values are positive throughout the envelope for this case. Furthermore, damping increases for low airspeed, which is the effect of induced drag due to increasing AoA.

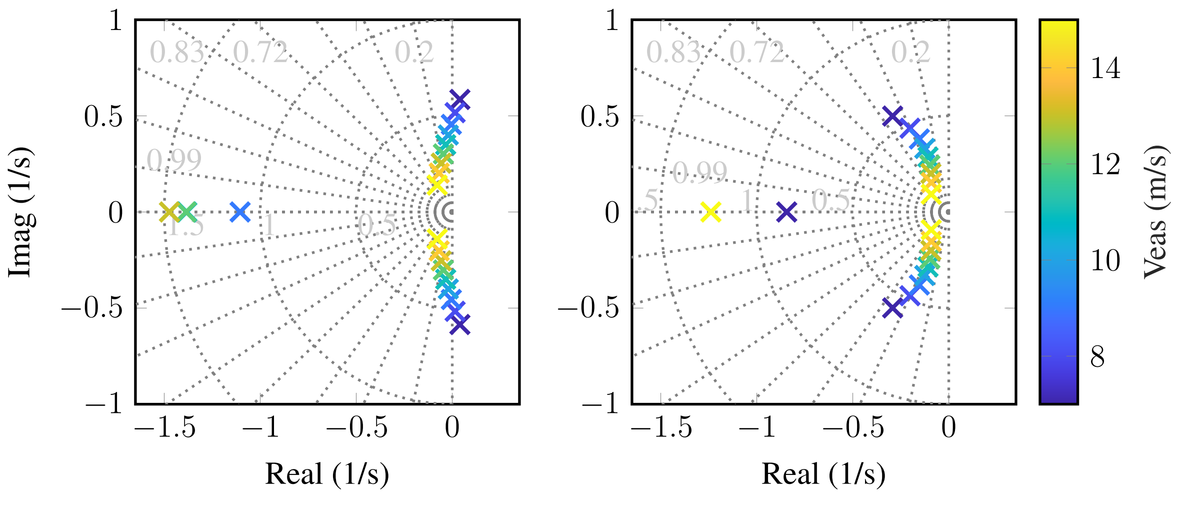

(a) Classic VLM (b) Updated VLM

Figure 5: Comparison of the Phugoid poles for classic and updated VLM models.

For the Dutch Roll, in Figure 6, the classic VLM version shows constant damping and an increase with airspeed in frequency. However, the induced drag in the right-hand graph of Figure 6 shows decreasing damping due to the mentioned effect of induced drag being approximately a second-order polynomial function of AoA. Again, for visualization purposes, only one altitude is selected, but the qualitative behavior holds for all altitudes.

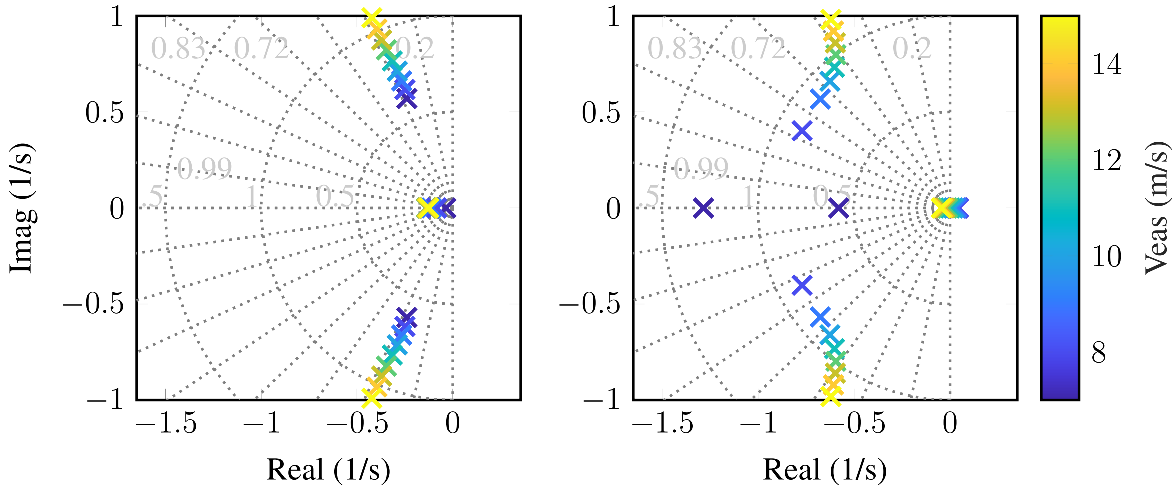

(a) Classic VLM (b) Updated VLM

Figure 6: Comparison of the Dutch Roll poles for classic and updated VLM models.

The updated VLM is used for control design, as it involves more realistic longitudinal and lateral aircraft dynamics, and thus, the robustness of the controller to remaining uncertainties in the model is increased.

3.2 Controller Architecture

For the design of the flight control laws, a cascaded architecture is used [13], consisting of an inner loop, which tracks the roll rate p and pitch rate q via a rate-command-attitude-hold (RCAH) control law, i.e., for zero input, the roll attitude Φ and pitch attitude Θ are maintained, which corrects for external (aerodynamic) disturbances. The outer cascade is the autopilot, which follows commands in the flight path angle (FPA) γ, equivalent airspeed (EAS) V_{eas}, and track angle χ. On the right-hand side within the block diagram in Figure 7, not included in the control software, AC MODEL denotes the nonlinear, flexible aircraft dynamics, including sensors and actuators. For the control design, the actuators and sensors are simplified as second-order dynamics and a delay approximation. From Figure 7, the following four main control modes, which will be assessed in the verification toolchain, can be derived:

1. Manual Mode: the pilot command is mapped to the control surfaces, and no protection algorithms are active.
2. Augmented Mode: the inner loop RCAH control law is active, and the pilot command is interpreted as pitch and roll rate command.
3. Flight Path Mode: the autopilot controls the flight path vector with the entries airspeed, FPA, and course angle command ($[V, \quad \gamma, \quad \chi]^T$), defined by the operator.
4. Managed Mode: a Flight Management System, which is not part of the FCSW, controls the aircraft trajectory and provides the flight path vector command.

For a change in mode, an additional cascaded loop is activated; thus, the activation order is set from inner to outer.Furthermore, this architecture inherently enables a a smooth, bumpless activation of each control loop. Additional controller components depicted in Figure 7 are the control allocation, which maps the inner loop command to the control surfaces. In this case, a fixed allocation is chosen, since the minimum weight requirement of the aircraft causes hardly any redundancy in the HALE aircraft, which would allow dynamic re-configuration. The Envelope Protection, however, tracks the airspeed and AoA during Augmented Mode operation and

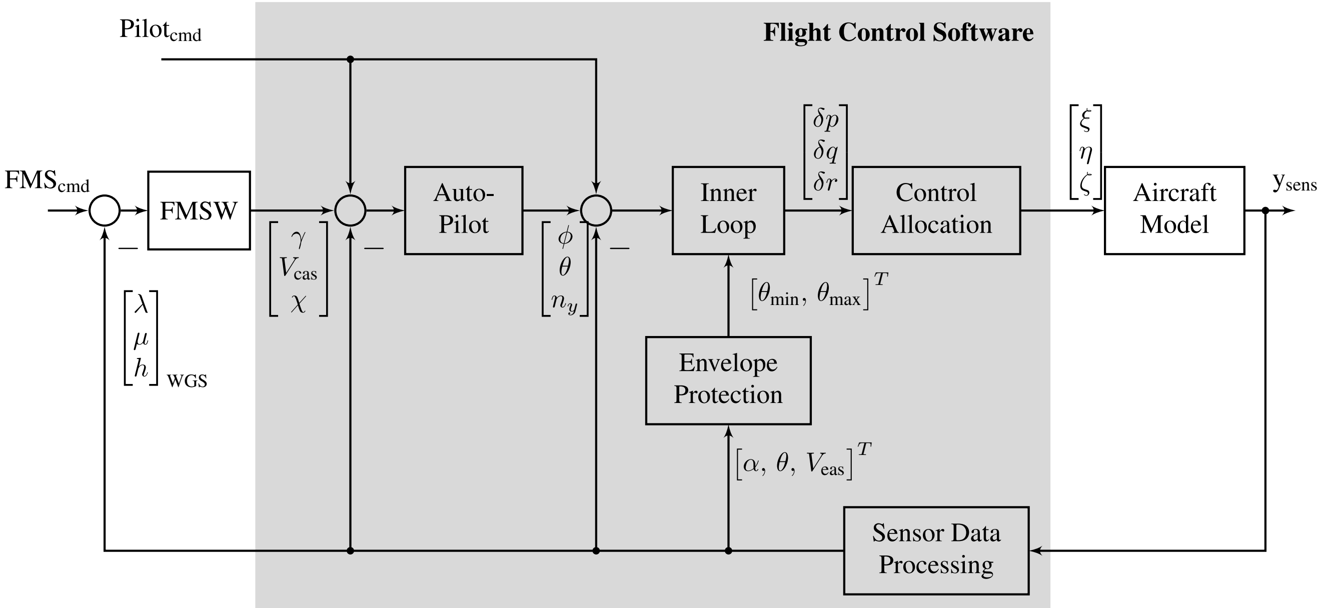

Figure 7: Controller architecture.

dynamically adjusts the pitch attitude limits in the inner loop according to the current airspeed vector. This function can be disabled as soon as the airspeed is managed by the autopilot. The design of the inner loop and autopilot control laws used structured H_∞ control and has been presented in [13].

3.3 Structured Mixed Sensitivity Control Design

The synthesis for the inner and outer loop control laws of the aircraft is conducted via mixed-sensitivity, fixed structure control design. This is motivated by the high-order linear aircraft models, which would cause a large number of states in a convex, full-order H_∞ design. Initial experiments showed that it is indeed possible to achieve adequate robustness and performance with a small number of gains and integrators.

For the control synthesis, the weighting scheme shown in Figure 8 was selected. Similar weighting architectures can also be found, e.g., in [15]. The control design approach works by shaping

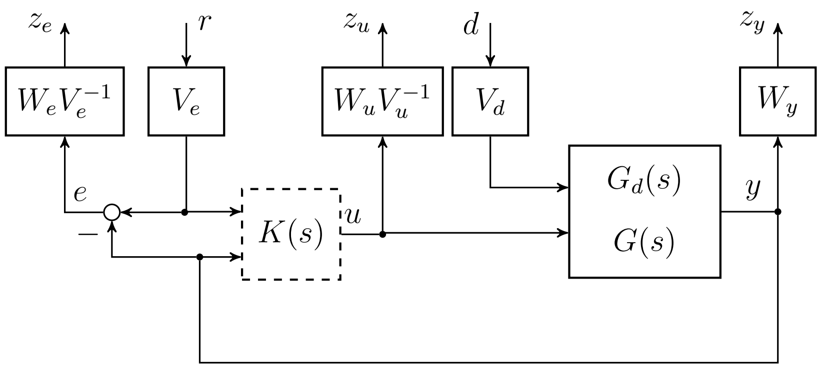

Figure 8: Weighting scheme for mixed-sensitivity control design.

the closed-loop sensitivity functions through minimization of the H_∞-norm, which is a common approach for control design in literature, see e.g. [14]. The considered plant $G(s)$ can be augmented by an explicit disturbance model $G_d(s)$, as depicted in Figure 8. The mixed sensitivity formulation is the weighted closed-loop system's H_∞-norm of the feedback interconnection in Figure 8 [14], which can be noted as follows:

$$\begin{bmatrix} z_e \\ z_u \\ z_y \end{bmatrix} = \begin{bmatrix} W_e V_e^{-1} & 0 & 0 \\ 0 & W_u V_u^{-1} & 0 \\ 0 & 0 & W_y \end{bmatrix} \begin{bmatrix} S & -SG_d \\ KS & KSG_d \\ GKS & SG_d \end{bmatrix} \begin{bmatrix} V_e & 0 \\ 0 & V_d \end{bmatrix} \begin{bmatrix} r \\ d \end{bmatrix}, \tag{27}$$

where $S = (I + GK)^{-1}$ denotes the output sensitivity function. The weighting scheme differentiates between frequency-dependent weights denoted by W and constant scaling factors denoted by V. These scaling factors are used to equalize the magnitudes of the individual in- and output channels of the plant.

The weight function W_e enforces the frequency requirements on the sensitivity function, i.e., tracking and disturbance rejection at low frequencies. The weight W_u shapes the control input u through KS. It can be used to enforce an appropriate roll-off of the controller K. The scale factors V_e, V_u, and V_d are used to set the maximum allowable control error, control effort, and disturbance, respectively. Additionally, the weight W_y is introduced to place weights on unmeasured signals, which are not fed back into the controller, i.e., the structural loads. The control design now has the goal to adjust the mentioned weights such that the design requirements listed in Table 1 are met. The tracking and control bandwidth can be directly set via the weights W_e and W_u, while the overshoot and robustness requirements are met after several iterations on the remaining weights and scale factors on disturbance and maximum control error. The final tuning result for the example of the longitudinal inner loop controller is shown in Figure 9. The remaining loops of the lateral controller and outer loop are tuned in a similar procedure, see [13, 16].

Table 1: Control Design Requirements.

Name	Target Value
Tracking bandwidth	$> 1\,\mathrm{rad/s}$
Maximum control bandwidth	$< 2\,\mathrm{rad/s}$
Max. overshoot	$< 10\,\%$
Disk-based gain and phase margin	$< 6\,\mathrm{dB}$ / $45\,\mathrm{deg}$

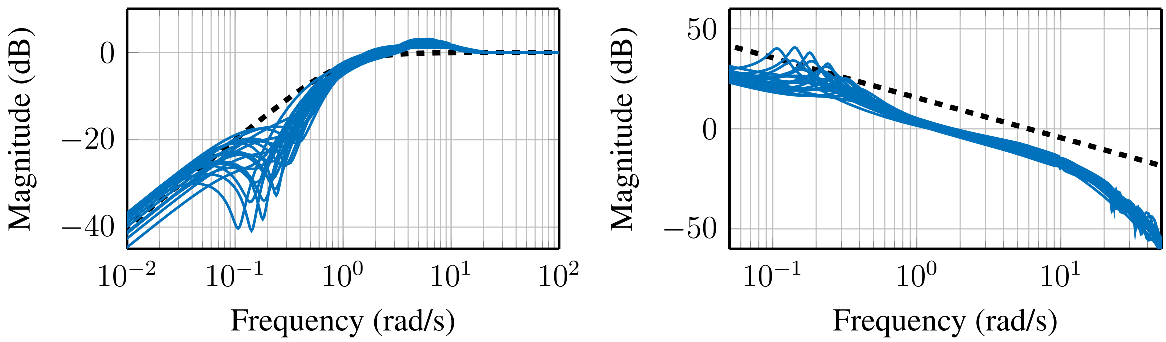

Figure 9: Longitudinal controller synthesis results, closed loop sensitivity (S)and control sensitivity (KS).

4 SIMULATION-BASED VERIFICATION

The initial verification of the controller was performed in the frequency domain to assess robustness margins using flexible aircraft models. In a second step, we move to verification by nonlinear simulation. A MC simulation and an optimization-based worst-case search use a SIL setup containing the high-fidelity aircraft model of the DLR *HAP-alpha* aircraft and the FCSW. The detailed clearance process is described in [17]. Figure 10 shows the closed-loop simulation model, which is an interconnection of the described aircraft model with the FCSW. The actuators are modeled as second-order dynamical systems with rate and position limits. The propulsion system is modeled as a first-order (PT-1) system for the motor, and the rotational speed n is converted to thrust via a detailed look-up table providing the thrust coefficient based on the propeller advance ratio $J = \frac{V_a}{n\,D}$ using the true airspeed V_a and the propeller diameter D. Sensor models are added to estimate the delay and noise of the original system so that an overall realistic high-fidelity aircraft model is achieved.

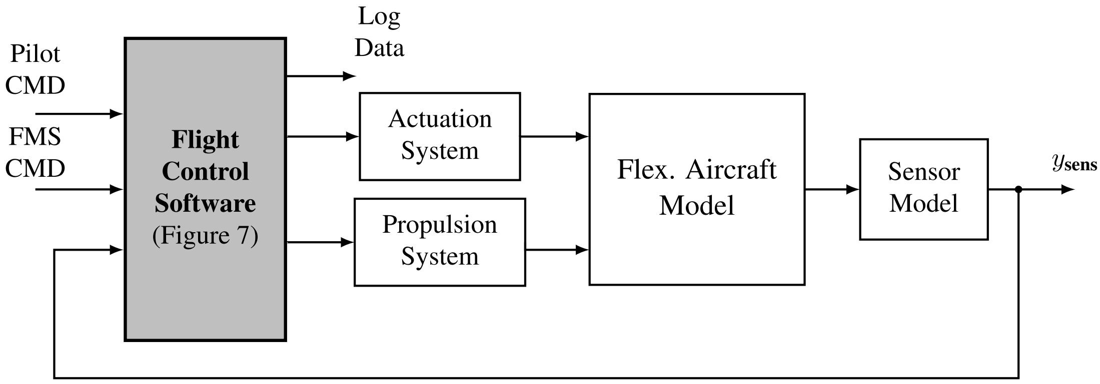

Figure 10: Block diagram of the SIL simulation environment.

4.1 Simulation Scenarios

The spatial wind velocity profile, v_g, of the discrete gust (1-cosine profile) is defined by Eq. (28) as specified by the certification requirements in EASA CS-25.341 [18]:

$$v_g = \frac{1}{2} U_0 \left(1 - \cos\left(\frac{2\pi x_j}{2H}\right)\right), \tag{28}$$

where U_0 is the gust design velocity. For the HALE aircraft, the expected worst-case amplitudes are reduced to account for the planned flight time in combination with the probability of a worst-case gust encounter. The spatial coordinate x_j denotes the distance of each panel ($j - \mathrm{set}$) to the gust velocity profile, v_g. The parameter H denotes the gust gradient and is defined between 9 and 107 meters according to [18]. The calculation of the aerodynamic loads due to the discrete gust is implemented as presented in [19, 20]. The result is applied to the model as an additional external load P_g^{ext}.

4.2 Monte Carlo Analysis

The flight clearance of the closed-loop aircraft is backed by a MC analysis, which uses the nonlinear simulator described above. The goal of this MC analysis is to verify the disturbance rejection properties and robustness of the FCSW against modeling uncertainties. For this reason, the MC allows a variation of the

(a) 1-cosine gust parameters (gust length, gust direction)
(b) aerodynamic damping and control effectiveness derivatives

which are shown in Table 2.

Table 2: Monte Carlo parameter distributions.

Name	Symbol	Distribution Type	[Min, Max]
Equivalent Airspeed	V_{eas}	uniform	$[9, 11]\,\mathrm{m/s}$
Gust gradient	h_{gs}	uniform	$[10, 80]\,\mathrm{m}$
Gust direction	ζ_{gs}	uniform	$[0, 360]\,\mathrm{deg}$
Factor on aerodynamic damping	C_{lp}, C_{mq}, C_{nr}	normal (1, 0.05)	$[0.75, 1.15]$
Factor on control surface effectiveness	$C_{l\xi}, C_{m\eta}, C_{n\zeta}$	normal (1,0.05)	$[0.75, 1.15]$

The MC simulation is run for 1000 samples, and each of the parameters is drawn from the respective probability distribution for the individual simulations. The analysis of the simulation focuses on the most important flight envelope parameters (for values, refer to Table 2):

(i) Maximum/minimum airspeed should stay within the narrow operational envelope (7 - $14\,\mathrm{m/s}$) for all disturbances
(ii) Maximum vertical and lateral load factors, n_z and n_y.
(iii) Maximum roll angle, Φ.
(iv) Maximum vertical tail root bending moment, $M_{\text{x, VT}}$, which has been found to cause critical torsional and bending loads in the fuselage.

For the stall and overspeed criteria, the metric of normalizing with the boundary values has been established:

$$M_s = \frac{V_s}{\min(V_{\text{eas}})} \tag{29}$$

for the stall speed, and

$$M_{ne} = \frac{\max(V_{\text{eas}})}{V_{ne}} \tag{30}$$

for the maximum, never-exceed, airspeed. This allows the definition of the minimum stall / overspeed margins in percent and is a useful optimization criterion for the optimizer running a worst-case search on the same model in addition to the MC simulation. For the current scenario, a minimum margin of $3\,\%$ was regarded as sufficient for the worst-case disturbance input. The results for the criteria are depicted in Figure 11. The stall margin stays just below the critical value of 0.97 (equal to the $3\,\%$ margin) across all 1000 samples. The maximum wing root bending load is exceeded in $0.5\,\%$ of the simulations.

4.3 Worst-Case Search

For the worst-case search, a global optimization technique is used since this promises high reliability in finding weaknesses compared to gridding and MC approaches [21, 22]. Furthermore, this process does not add conservatism (in contrast to, e.g., linear methods such as μ-analysis), works on the full nonlinear model, and thus the optimization approach is very flexible concerning the problem type. The worst-case aircraft parameter set found can be used to improve the FCSW parameters further, or to identify weaknesses in the flight envelope and constrain the envelope for the first flight.

Formulation of a Global Optimization Problem. To utilize optimization methods, the clearance problem must be expressed as a scalar objective function $c(p, d)$ with optimization parameters p that are uncertain or variable during operation (e.g., aerodynamic coefficients, wind or aircraft mass, inertia, speed, height, etc.) and discrete conditions d (e.g., aircraft configuration,

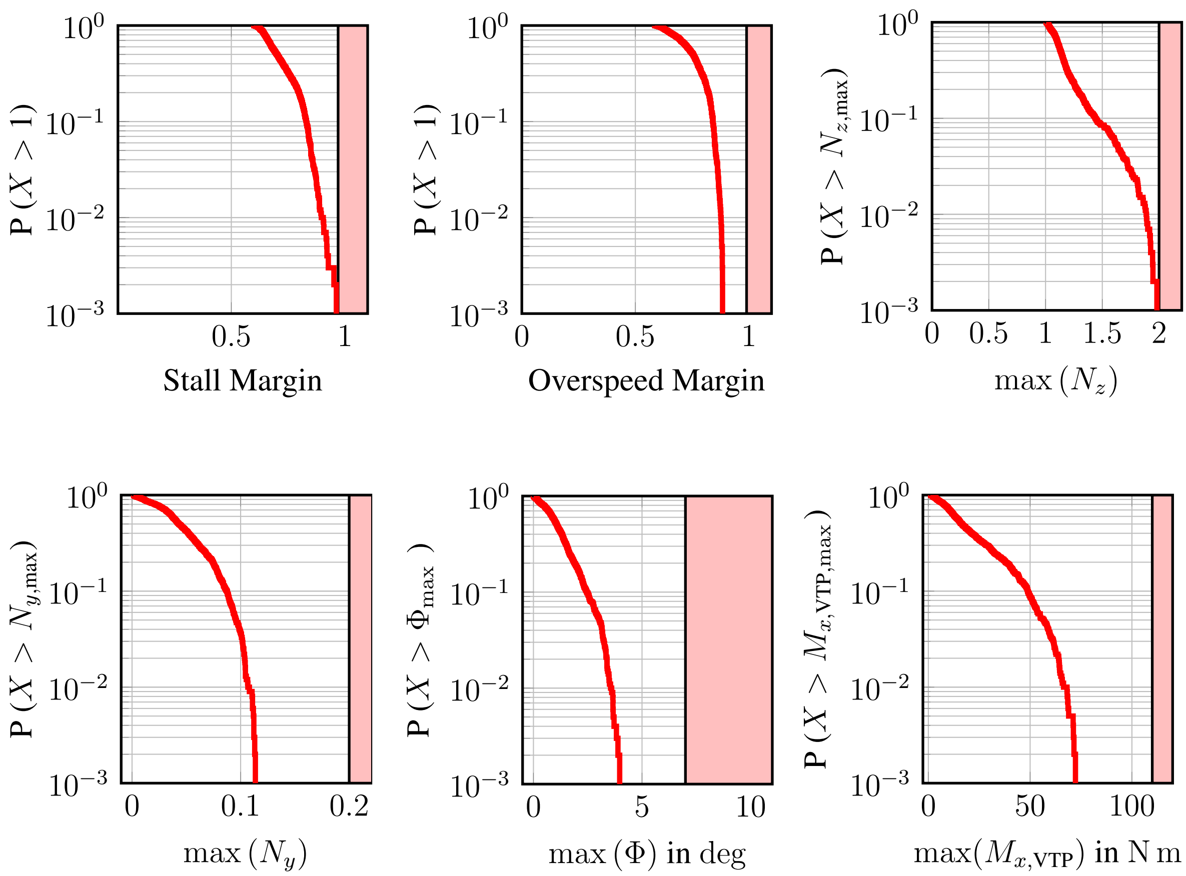

Figure 11: Monte Carlo analysis results: probability of exceedance of critical values for different flight envelope parameters in 1000 simulations.

landing gear settings, etc.). The components of p are assumed to be bounded and continuously varying over known intervals, defining a hyperbox P. The clearance problem can now be formulated as a maximization problem. Let $c_0(d)$ be an upper acceptable value for c, then

$$c_{\max}(d) = \max_{p \in P} \left(c(p, d) \right) \tag{31}$$

is a measure of the clearance performance. We assume that the clearance requirement is fulfilled for condition d if $c_{\max}(d) \leq c_0(d)$; otherwise, the criterion is not cleared.

For the worst-case search, the MOHGA algorithm available within the DLR Multi-Objective Parameter Synthesis (MOPS) toolbox [23] is used. MOHGA is primarily developed to solve multi-objective optimization problems, i.e., to find approximations of the Pareto front. For this, MOHGA applies a hybrid solution of a non-dominated sorting algorithm, similar to the NSGA-II algorithm described by Deb et al. [24], which is combined with a pattern search algorithm. In the case of constraints, infeasible solutions are always considered worse than feasible ones.

Worst-Case Search Results. For the free parameters within the worst-case search, the same criteria are selected as within the MC simulation above (Section 4.2):

- the maximum roll attitude $c_1 = \max(|\Phi|)$
- maximum lateral load factor $c_2 = \max(|n_y|)$
- maximum vertical load factor $c_3 = \max(n_z)$
- margin to never-exceed airspeed V_{ne}, $c_4 = \max(\frac{V_{\mathrm{eas}}}{V_{\mathrm{ne}}})$

- margin to stall speed V_s, $c_5 = \max(\frac{V_\mathrm{s}}{V_\mathrm{eas}})$
- maximum vertical tail bending moment $c_6 = \max(|M_{\mathrm{x,\,VT}}|)$

The selection aims to check for critical conditions with regard to the integrity of the aircraft's structure and stall risk. All six criteria are formulated in a manner such that low values are denoted as GOOD, and thus, the anti-optimization problem shall maximize each of the six criteria. The result of this anti-optimization problem for the HALE aircraft is shown in Table 3. In the table, the column "WC value" designates the worst case found for the full parameter space. For the column "WC FT", the parameter space was constrained to the envelope which is applicable in the planned flight testing. Here, the altitude is limited to $500\,\mathrm{m}$ and the trim airspeed to $10\,\mathrm{m/s}$. The results in Table 3 show that the limits for roll attitude, load factor (n_z), stall, and

Table 3: Worst-case search results.

	Unit	WC value	WC FT	Limit
$c_1 = \max(\lvert\Phi\rvert)$	deg	8.6	5.5	7
$c_2 = \max(\lvert n_y\rvert)$	g	0.178	0.12	0.2
$c_3 = \max(n_z)$	g	2.39	2.0	2
$c_4 = \max(\frac{V_\mathrm{eas}}{V_\mathrm{ne}})$	-	1.08	0.89	0.97
$c_5 = \max(\frac{V_\mathrm{s}}{V_\mathrm{eas}})$	-	1.04	0.89	0.97
$c_6 = \max(\lvert M_{\mathrm{x,\,VT}}\rvert)$	N m	103	82	110

overspeed margin, could be violated by the algorithm (marked in red in Table 3). However, this was in the case for the full flight envelope and is discussed subsequently. For a second run, with constrained envelope boundaries, the optimization-based worst-case search could not violate any of the flight envelope parameters.

4.4 Discussion and Implications for Flight Testing

The obtained results for the MC analysis must be interpreted in the context of underlying probabilities: the investigated scenarios are based on a worst-case gust, which is expected to happen once in the lifetime of the aircraft. Furthermore, at the same time, a deviation in aerodynamic model parameters was investigated. This scenario is already a very rare event, which is then multiplied by the given probability of exceedance in Figure 11. Therefore, the total probability of envelope exceedance is calculated as $p_\mathrm{tot} = p_\mathrm{wc} p_\mathrm{mc}$, where p_tot is the total risk, p_wc is the risk of experiencing any worst-case gust condition, and p_mc is the risk of envelope exceedance found in the MC for all worst-case gusts. Since the aircraft is to be operated at a very low number of hours, an upper bound for such an estimate could be, e.g., 1×10^{-3} for the value of p_wc, which would result in a total exceedance boundary of 1×10^{-6} for the MC results. However, the MC results led to a further improvement of the lateral control law. This step is executed to push the worst-case structural loads for the nominal aircraft configuration (without model uncertainties, but for all considered worst-case gusts) below the critical limits.

For the optimization-based worst-case search results, the violations in velocity margins were found for cases with a trim-airspeed $1\,\mathrm{m/s}$ below the minimum operational speed (for the stall margin violation). For the never-exceed speed violation, the trim speed was $1\,\mathrm{m/s}$ above the maximum operational speed. This $1\,\mathrm{m/s}$ exceedance of operational condition has been selected as a safety margin and thus is the limit of the trim airspeed parameter during the worst-case search. The third violation for the load factor was found for a relatively short vertical gust (H_{gs} =$14\,\mathrm{m}$) as well as an equivalent airspeed $1\,\mathrm{m/s}$ above the operational limit, and a simultaneous deviation in longitudinal stability parameters.This has been further discussed in [17] and for future work these results will lead to improvements in controller tuning. For the column with worst-case search results specifically for the first flight in Table 3, the limits are all adhered and the current FCSW version is cleared for flight testing.

5 CONCLUSION

This paper presented a robust flight control design methodology for the German Aerospace Center's High-Altitude Platform configuration, *HAP-alpha*. The challenges posed by the spectral overlap between rigid-body and structural modes, typical of lightweight, large-wingspan stratospheric vehicles, are addressed by integrating a fully flexible aircraft model into the control synthesis loop. Furthermore, adaptations to the VLM aerodynamics deliver more realistic dynamic behavior in the longitudinal and lateral axes. This is achieved by using a cross product accounting for the tilted lift vector. The control laws are synthesized via structured H_∞ optimization. This synthesis process inherently delivers a robust control design. Further verification results, including nonlinear SIL simulations, confirmed the controller's effectiveness in tracking reference commands while rejecting structural oscillations. Furthermore, the extensive clearance process, encompassing both statistical MC simulations and optimization-based worst-case load searches, demonstrated that the system satisfies critical safety margins under worst-case atmospheric disturbances in the nominal model configuration. However, when model uncertainties, gust parameters, and trim airspeed and altitude are in a worst-case configuration, the safety margins are violated for some of the parameters. These findings were deemed acceptable for a first flight of the platform, since several worst cases (model uncertainty, edge of the flight envelope, and a once per lifetime worst case gust) must coincide for the aircraft to leave its safe flight envelope. These results are therefore considered acceptable for a first flight but will inform future robustness improvements. The presented clearance setup thus verifies the baseline flight control system and clears it for initial flight testing. In conclusion, the paper provides an extensive framework for the flight control design and verification of highly flexible HALE aircraft.

6 ACKNOWLEDGEMENTS

The research leading to these results is part of the DLR *HAP-alpha* project. The authors would like to thank the colleagues at the DLR Institutes of Aerodynamics and Flow Technology, Lightweight Systems, Aeroelasticity, and Flight Systems for their contributions towards the flight dynamics model of the *HAP-alpha* aircraft.

7 REFERENCES

[1] Apkarian, P. and Noll, D. (2006). Nonsmooth h∞ synthesis. *IEEE Transactions on Automatic Control*, 51(1), 71–86. doi:10.1109/TAC.2005.860290.

[2] Voß, A., Koch, C., Niemann, S., et al. (2022). Transition from preliminary to detailed design of a highly elastic solar electric aircraft. In *International Forum on Aeroelasticity and Structural Dynamics (IFASD)*.

[3] Hasan, Y. J., Roeser, M. S., Hepperle, M., et al. (2022). Flight mechanical analysis of a solar-powered high-altitude platform. *CEAS Aeronautical Journal*, 14(1), 201–223. ISSN 1869-5590. doi:10.1007/s13272-022-00621-2.

[4] Waszak, M. R. and Schmidt, D. K. (1988). Flight dynamics of aeroelastic vehicles. *Journal of Aircraft*, 25(6), 563–571. ISSN 1533-3868. doi:10.2514/3.45623.

[5] Kier, T. M., Looye, G., and Hofstee, J. (2005). Development of aircraft flight loads analysis models with uncertainties for pre-design studies. In *Proc. of IFASD 2005, International Forum on Aeroelasticity and Structural Dynamics*.

[6] Kier, T. (2022). An integral flexible aircraft model for optimal control surface scheduling of manoeuvre load alleviation and wing shape control functions. In *International Forum on Aeroelasticity and Structural Dynamics*.

[7] Bisplinghoff, R. L., Ashley, H., and Halfman, R. L. (2013). *Aeroelasticity*. Dover Publications, Incorporated. ISBN 9780486132433.

[8] Hedman, S. (1965). Vortex Lattice Method for Calculation of Quasi Steady State Loadings on Thin Elastic Wings. Tech. Rep. Report 105, Aeronautical Research Institute of Sweden.

[9] Pistolesi, E. (1937). Betrachtungen über die gegenseitige Beeinflussung von Tragflügelsystemen. In *Gesammelte Vorträge der Hauptversammlung 1937 der Lilienthal Gesellschaft*.

[10] Rodden, W. P., Harder, R. L., and Bellinger, E. D. (1979). Aeroelastic Addition to NASTRAN. Tech. Rep. NASA CR-3094, NASA.

[11] Kier, T. M. and Looye, G. H. N. (2009). Unifying manoeuvre and gust loads analysis. In *International Forum on Aeroelasticity and Structural Dynamics*.

[12] Harder, R. and Desmarais, R. (1972). Interpolation Using Surface Splines. *Journal of Aircraft*, 9(2), 189–191. doi:10.2514/3.44330.

[13] Weiser, C. and Ossmann, D. (2022). Baseline flight control system for high altitude long endurance aircraft. In *AIAA SciTech Forum*. American Institute of Aeronautics and Astronautics. doi:10.2514/6.2022-1390.

[14] Skogestad, S. and Postlethwaite, I. (2005). *Multivariable Feedback Control*. John Wiley. ISBN 9780470011676.

[15] Theis, J., Pfifer, H., and Seiler, P. (2020). Robust modal damping control for active flutter suppression. *Journal of Guidance, Control, and Dynamics*, 43(6), 1056–1068. doi:10.2514/1.g004846.

[16] Weiser, C., Ossmann, D., and Pfifer, H. (2023). Robust path-following control for high-altitude long-endurance aircraft. *Journal of Guidance, Control, and Dynamics*, 46(7), 1416–1424. doi:10.2514/1.g007326.

[17] Weiser, C. (2025). Verification and clearance of a flight control system for high altitude long endurance aircraft. In *2025 IEEE Aerospace Conference*. pp. 1–11. doi:10.1109/AERO63441.2025.11068608.

[18] European Aviation Safety Agency (EASA) (2023). Certification Specifications and Acceptable Means of Compliance for Large Aeroplanes CS-25.

[19] Schulz, S. and Ossmann, D. (2022). Estimation of global structural aircraft loads due to atmospheric disturbances for structural fatigue estimation. In *International Forum on Aeroelasticity and Structural Dynamics (IFASD)*.

[20] Hoblit, F. M. (1988). *Gust Loads on Aircraft: Concepts and Applications*. American Institute of Aeronautics and Astronautics. doi:10.2514/4.861888.

[21] Joos, H.-D. (2012). Worst-case parameter search based clearance using parallel nonlinear programming methods. In A. Varga, A. Hansson, and G. Puyou (Eds.), *Optimization-Based Clearance of Flight Control Laws: A Civil Aircraft Application*. Springer Berlin Heidelberg. ISBN 978-3-642-22627-4, pp. 149–159. doi:10.1007/978-3-642-22627-4_8.

[22] Varga, A. (2002). Optimisation-based clearance. In C. Fielding, A. Varga, S. Bennani, and M. Selier (Eds.), *Advanced Techniques for Clearance of Flight Control Laws*. Springer Berlin Heidelberg. ISBN 978-3-540-45864-7, pp. 107–117. doi:10.1007/3-540-45864-6_7.

[23] Joos, H.-D. (2002). A multiobjective optimisation-based software environment for control systems design. In *Proceedings. IEEE International Symposium on Computer Aided Control System Design*. pp. 7–14. doi:10.1109/CACSD.2002.1036921.

[24] Deb, K., Pratap, A., Agarwal, S., et al. (2002). A fast and elitist multiobjective genetic algorithm: Nsga-ii. *IEEE Transactions on Evolutionary Computation*, 6(2), 182–197. doi:10.1109/4235.996017.

COPYRIGHT STATEMENT